Hexagonal microlasers based on organic dyes in nanoporous crystals

I. Braun[2], G. Ihlein[1], F. Laeri[3],*, J.U. Nöckel[4], G. Schulz-Ekloff[2], F. Schüth[1], U. Vietze[3], Ö. Weiß[1], D. Wöhrle[2]

[1] Max-Planck-Institut für Kohlenforschung, 45470 Mülheim, Germany
(Fax: +49-208/306-2995)
[2] University of Bremen, 28334 Bremen, Germany
(Fax: +49-421/218-4935)
[3] Darmstadt University of Technology, 64289 Darmstadt, Germany
(Fax: +49-6151/163-022)
[4] Max-Planck-Institut für Physik komplexer Systeme, 01187 Dresden, Germany
(Fax: +49-351/871-1999)

Abstract. Molecular sieves, such as nanoporous $AlPO_4$-5, can host a wide variety of laser active dyes. We embedded pyridine-2 molecules as a representative of a commercially available dye which fits into the channel pores of the host matrix. Many efficient dye molecules, such as rhodamines, do not fit into the pores. But modifying the structure of the dyes to appear like the used templates allows us to increase the amount of encapsulated dyes. The properties of resulting microlasers depend on size and shape of the microresonators, and we discuss a model for microscopic hexagonal ring resonators. In terms of pump needed to reach lasing threshold molecular sieve microlasers are comparable to VCSELs. For dyes that fit into the pores we observed a partial regeneration of photo-induced damage.

PACS: 42.55.Sa; 42.55.Mv; 61.43.Gt; 61.66.Fn

In recent years dye laser emission from crystalline materials attracted considerable interest [1, 2]. At the same time in solid-state dye lasers based on polymer matrices single-mode operation at high peak powers was demonstrated [3], and photodegradation processes were identified [4]. Recently, we reported on microscopic dye lasers, in which the active molecules were embedded in crystallographically defined nanometer-size pores of molecular sieves [5]. In the past, such nanoporous materials, for example zeolites, proved to be pertinent especially for the catalysis in oil refining and petrochemistry, where they are used in huge amounts. It is only recently that applications of this class of porous crystalline material have been discussed in an optical context. In fact, molecular sieves can be used to host a wide variety of optically relevant guests, such as atoms, ions, or molecules [6].

Sieves with tubular or channel pores, in particular, can act as an ordering framework for guest molecules [7]. For optical applications it is possible to exploit thus distinct spatial symmetries in the arrangement of organic molecules, so enhancing, for example, the second-order nonlinear susceptibility of the compound [8], or admitting anisotropic Förster energy migration [9]. Nanoporous crystals were also studied as hosts for luminophores [10], pigments [11], optical switches [12] or dye lasers [5]. In the following we report about the novel emission properties of hexagonal monolithic microresonators realized with dyes intercalated in molecular sieve microcrystals, and the photostability of these systems.

1 Material

1.1 Host crystal

Molecular sieve materials are characterized by a crystallographically defined framework of regularly arranged pores. In Table 1 we list some sieves, which, owing to their large diameters of channel pores, are suitable for hosting optically effectual organic molecules. Among the listed materials especially the aluminophosphate $AlPO_4$-5 (molecular mass 1463.4 g/mol) can be synthesized with good optical transparency and low internal scattering losses. Its channel pores exhibit a diameter of 0.73 nm, which is large enough to accommodate suitable organic dye molecules.

$AlPO_4$-5 crystals are crystallized from aqueous or alcoholic solutions under hydrothermal conditions, with the addition of an organic structurizing agent, called template. The template, tri-n-propylamine in our case, is necessary to direct the synthesis towards the desired structure. The preferred pH range for the synthesis is mildly acidic to mildly basic. The most utilized source of phosphore is orthophosphoric acid, and the most studied sources of aluminum are pseudoboehmite and alkoxides [14]. Single crys-

*Corresponding author.
Present address: Institute of Applied Physics, Darmstadt University of Technology, 64289 Darmstadt, Germany
(Fax: +49-6151/163-022, E-mail: franco.laeri@physik.tu-darmstadt.de)

Table 1. Lattice constants and free pore diameter ϕ of molecular sieves with linear channels [13]

	a/nm	b/nm	c/nm	ϕ/nm
		hexagonal		
mazzite	1.84		0.76	0.74
AlPO$_4$-5	1.34		0.84	0.73
zeolite L	1.84		0.75	0.71
gmelinite	1.38		1	0.7
offretite	1.33		0.76	0.68
CoAPO-50	1.28		0.9	0.61
cancrinite	1.28		0.51	0.59
		orthorhombic		
AlPO$_4$-11	1.35	1.85	0.84	0.63×0.39
mordenite	1.81	2.05	0.75	0.70×0.65

tals with nearly perfect morphology were grown using hydrofluoric acid [15]. With a specially prepared and aged aluminum hydroxide gel crystal sizes around 1 mm in c-axis direction were obtained [16], whereas microwave heating proved to increase the crystallization rates by more than one order of magnitude [15, 17].

Pure AlPO$_4$-5 crystals are optically transparent from below 400 nm to above 800 nm ($n_{500\,nm} = 1.466$), and after removing the template (usually by heating/calcinating) they exhibit practically no birefringent properties. X-ray patterns revealed systematic absences which are consistent with space group P$\frac{6}{m}cc$ as well as P6cc, whereby, however, the latter implies a polar nature of AlPO$_4$-5 single crystals: In fact, the 4 in the formula is the result of the strict alternation of Al and P in the tetrahedral nodes of the framework, which prevents the corner-sharing oxygen tetrahedra occuring with odd numbers, and which leads to an alternating stacking of Al and P in the direction of the channels (c axis). This is assumed to cause the crystallographic polar nature [18] of the framework [19]. The macroscopic polar nature of AlPO$_4$-5 single crystals has been proven recently in scanning pyroelectric microscopy investigations [20]. There it was also observed that AlPO$_4$-5 crystals are usually twinned. The murky stripes inside the pyridine 2-loaded crystals shown in Fig. 1 and their slightly bowed side faces could well be a result of this kind of twinning. It is not clear, however, to what extent such twinning should affect the optical properties relevant for the effects discussed here.
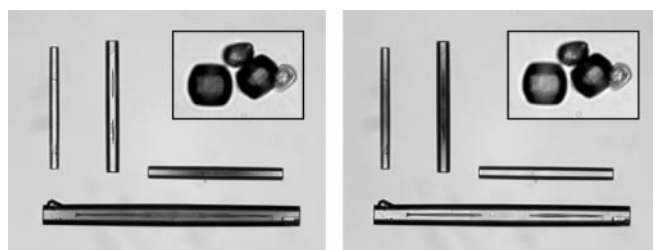

Fig. 1. Transmission micrographs of the dichroism in dye-loaded AlPO$_4$-5 crystals; the rod-shaped crystals contain about 0.1 wt % or 1 pyridine-2 molecule per 260 unit cells, while the barrel-shaped ones (shown in the inset) enclose rhodamine BE50 (about 0.5 wt % or 1 molecule per 75 unit cells). Only the polarization component parallel to the optical transition moment of the molecules is absorbed. In the rod-shaped crystal the pyridine-2 dyes are completely aligned, whereas with the rhodamine BE50 dye in the barrel-shaped crystals we observe only a weak dependence of the color upon the incident polarization. *Left*: incident light horizontally polarized; *Right*: incident light vertically polarized

1.2 AlPO$_4$-5/*pyridine* 2 *compound*

The compounds were synthesized following a procedure in which the dye 1-ethyl-4-(4-(p-dimethylaminophenyl)-1,3-butadienyl)-pyridinium perchlorate (cf. Fig. 2) (pyridine 2 [21]) is added to the template or to the aluminum hydroxide suspension [22–24]. After 1 h of hydrothermal synthesis dark red crystals with a length of up to 100 μm were obtained. The crystals were refluxed in ethanol for 4 h whithout any detectable extraction of dye. The slim, linear dye molecules fit snugly into the 0.73-nm-wide channel pores of the nanoporous AlPO$_4$-5 host, resulting in an ordered compound material, in which the dye molecules are all aligned along the crystal c-axis. As a consequence the compound exhibits strong dichroism, and the emitted fluorescence light is polarized parallel to the c axis. This is documented in Fig. 1. It is also observed that with the inclusion of pyridine 2 the entire compound acquired pyroelectric properties and an optical second-order susceptibility [5].

Depending on the dye content different morphologies of crystals are observed. Regular hexagonal crystals with a rod-like form, as for example the ones shown in Fig. 1, were obtained when the dye content was low, around 0.1 wt % or 1 molecule per 260 unit cells. At higher concentrations the dye accumulated in the middle of the crystal, and the morphology was severely disturbed. At dye content $\gtrsim$ 0.2 wt % crystals with a characteristic fascicular shape resulted; cf. Fig. 3. Given the small size of the crystals we had to determine the dye content by chemically dissolving them. With this method, however, it was not possible to accurately determine the spatial distribution of the dye. We therefore evaluated the content qualitatively by comparing the depth of the color. It was only with these fascicled pyridine-2-loaded crystals that we ob-
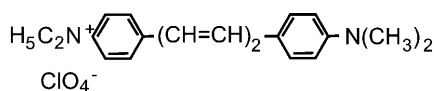

Fig. 2. Structure formula of the dye 1-ethyl-4-(4-(p-dimethylaminophenyl)-1,3-butadienyl)-pyridinium perchlorate (pyridine 2 [21]); molecular mass 378.9 g/mol
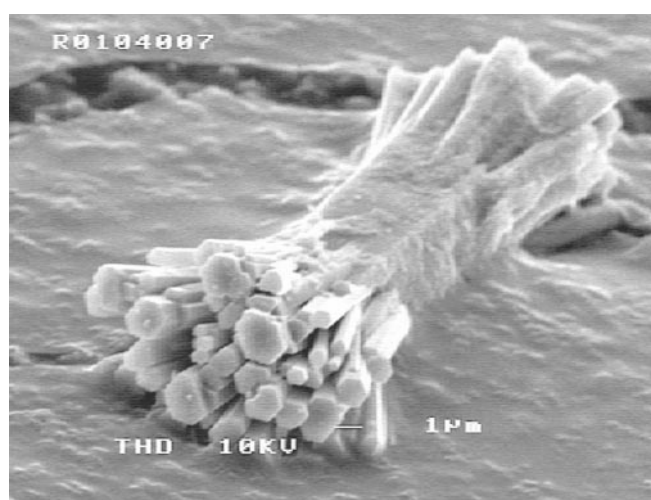

Fig. 3. Morphology of typical pyridine 2/AlPO$_4$-5 crystals with lasing properties

served laser emission. Apparently the low concentration of dye in the undisturbed rod-shaped crystals did not spoil the growth but on the one hand was not sufficient to provide the necessary optical gain for compensating all losses.

1.3 AlPO$_4$-5/rhodamine BE50 compound

The synthesis gel was prepared according to recipes [18, 25] modified for the purpose of crystallization inclusion of dyes [26]. To a suspension of 61.6 mmol Al$_2$O$_3$ (8.44 g; Pural SB, Condea Chemie) as aluminum source and 75 g deionized water, 61.6 mmol P$_2$O$_5$ (14.20 g phosphoric acid; 85 wt%, p.a. Merck) in 11.3 g deionized water was added under mechanical stirring. After 5 min a uniform gel formed and then 92.4 mmol tripropylamine (13.25 g Prop$_3$N, Merck) was added slowly. Subsequently, the appropriate amount (0.1–10 mmol) of the dye powder was mixed with the gel. The new derivative rhodamine BE50 (ethanaminium, N-[6-(diethylamino)-9-[2-(N, N-dimethyl-3-amino-1-proproxy-carbonyl) phenyl]-3H-xanthen-3-ylidene]-N-ethyl-chloride; cf. Fig. 4) was synthesized by esterification of rhodamine B (Rh B) with 3-dimethylamino-1-propanol [27]. It was shown that the concentration of rhodamine BE50 (Rh BE50) achievable by crystallization inclusion in AlPO$_4$-5 exceeds the possible Rh B concentration by a factor of 3 − 4. This was attributed to the different molecule structures, i.e., to the zwitterionic nature of Rh B on one hand, and to the additional positive charge of a protonated aliphatic amino group of Rh BE50 on the other hand [27]. The latter molecules with the localized positive charge are more compatible with the AlPO$_4$-5 framework than the delocalized charge of Rh B. As a consequence we observe that at the same dye concentration Rh BE50 inclusion leads to a better crystal morphology than Rh B inclusion [28]. The synthesis of the Rh BE50/AlPO$_4$-5 crystals was performed by microwave heating [29], which has proven to be superior in respect of avoiding damage of sensitive dyes such as coumarines [11] as well as in reducing the time of synthesis [27].

Unlike the pyridine-2 molecules, which with a diameter of 0.6 nm fit into the 0.73-nm-wide pores of the AlPO$_4$-5 host, the Rh BE50 molecules with dimension of 0.91×1.36 nm must be accommodated in defect sites (mesopores) of the host crystal. Remarkably, up to concentrations of 1 molecule per 75 unit cells this remains without any visible negative consequences for the crystal morphology, as is documented in Fig. 5.
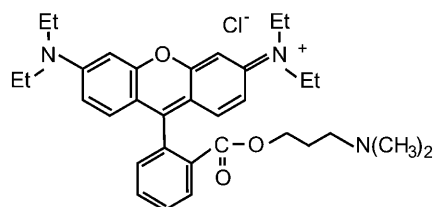
Fig. 4. Structure formula of the new dye rhodamine BE50 (ethanaminium, N-[6-(diethylamino)-9-[2-(N, N-dimethyl-3-amino-1-propoxycarbonyl)-phenyl]-3H-xanthen-3-ylidene]-N-ethyl-chloride) molecular mass 564 g/mol [27]
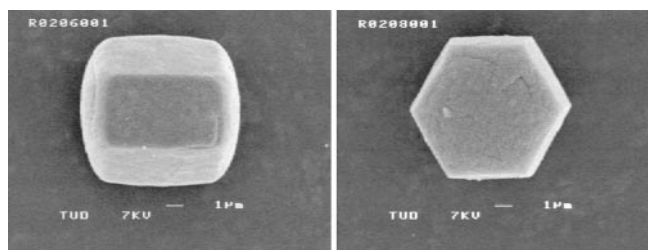
Fig. 5. Morphology of typical rhodamine BE50/AlPO$_4$-5 crystals with lasing properties; dye content ca. 0.5 wt% or 1 dye molecule per 75 unit cells

In Fig. 1 the dichroic properties of the compound are illustrated. In comparison with the pyridine-2/AlPO$_4$-5 compound, the dichroism of the Rh BE50 compound is reduced and the fluorescence emission is partially polarized. Thus it is inferred that the anisotropy of the host structure does not fully carry through the mesopores, and thus the guest molecules are only weakly aligned.

2 Microresonator structure

As is visible in Fig. 1 — and as the polarization of the emitted fluorescence of the compounds indicates — the absorption, as well as the emission dipole moment of the included dyes are oriented preferentially along the crystal c-axis (complete orientation in the pyridine-2/AlPO$_4$-5 compound). As dipole emission along the dipole axis is not possible, the emission parallel to a plane perpendicular to the prevailing dipole orientation (i.e. the hexagonal axis) is enhanced. Here a bundle of emission directions meets the condition for total internal reflection (TIR) at the hexagonal side faces inside the crystal. In a whispering-gallery-mode-like way the corresponding emission can circulate sufficiently often to accumulate the gain required to overcome the lasing threshold; cf. Fig. 6 in which this intuitive model is illustrated for a particular ray bundle of high symmetry. However, with resonator sizes in the order of a few wavelengths, as discussed here, the ray picture does not represent the field modes even in a qualitatively correct way. For example the ray picture insinuates a mode concentration in the center of the faces and field-free corners. However, this is not consistent with the experimental
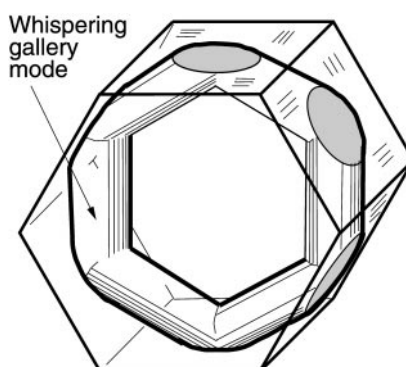
Fig. 6. Naïve ray picture interpretation of a whispering-gallery laser mode inside a hexagonal prism. In the following it is shown that for prisms with sizes of a few wavelengths this picture has to be modified

evidence, which clearly shows that the emission occurs at the corners; cf. Fig. 13. In fact, for dielectric resonator structures a few wavelengths large with TIR field confinement a wave model has to be worked out.

2.1 Ray picture

The main feature that distinguishes the hexagonal resonator from other common whispering-gallery-type cavities such as microdroplets [30] or semiconductor disk lasers [31, 32], is that the latter do not exhibit sharp corners and flat sides. Portions of the boundary in convex resonators can act as focusing or defocusing elements, but the straight sides of a hexagon are neither one nor the other. The hexagon in fact constitutes a self-assembled realization of a *pseudointegrable* resonator [33]: for a polygon with precisely 120° angles between adjacent sides, any ray lauched at some angle to the surface will go through only a finite number of different orientations [34], just as in the more familiar rectangular resonator where there are at most two non-parallel orientations for any ray path. In the hexagon, a ray encounters the interface with at most three different angles of incidence. Despite this apparent simplicity, there exists no orthogonal coordinate system in which the wave equation for the hexagonal cavity can be solved by separation of variables. This property of non-integrability is shared by wave equations whose classical (short-wavelength) limit exhibits chaos. However, ray paths in the hexagon display a degree of complexity that cannot be classified as chaotic, and hence the term pseudointegrability has been coined for these systems. The ray–wave duality in "billiards" of this type has to be addressed in order to explain how they can support whispering-gallery modes that emit at the corners.

In order to characterize the sample size, one can specify either the radius R of the hexagon at the corner points or — more conveniently — the width over flats (WoF) satisfying the relation $R = WoF/\sqrt{3}$. The closed ray path underlying Fig. 6 is only one member of an infinite family of periodic orbits of the hexagon billiard that all have the same length, $L = 3 \times WoF$, as shown in Fig. 7. Long-lived cavity modes should be expected only if the corresponding rays satisfy the condition of TIR at the interface, $\sin \chi > 1/n$, where χ is the angle of incidence with respect to the surface normal. This is true for the orbits of Fig. 7. In a naive ray approach one would furthermore obtain the spectrum of modes by requiring an integral number of half wavelengths to fit into L, leading to constructive interference on a round-trip. As we shall see shortly, this estimate is justified, even though a proper treatment of the ray–wave connection has to take in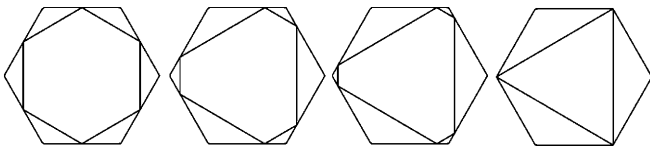to account that any given mode is in fact made up of a whole *family* of different ray paths. The ultimate breakdown of the ray model, however, is illustrated in Fig. 7 by the degenerate ray orbit hitting the corners where the classical laws of refraction and reflection become undefined.

2.2 Wave picture: spectral properties

Because the hexagonal faces are neither focusing nor defocusing, there is no obvious way of determining the weight that should be given to individual members of a ray family as depicted in Fig. 7, in order to predict the spatial structure of the resulting mode. Full solutions of Maxwell's equations have therefore been carried out for the TM polarized modes of a dielectric hexagonal prism, using methods previously applied in [31, 32]. In anticipation of the experimental spectra to be discussed in Sect. 3, attention here is focused on three different sample sizes, with WoF 4.5 μm, 7.5 μm, and 22 μm. The aim is to understand the observed laser line spacings and the emission directionality. Comparison of the calculated and observed linewidths will not be attempted because the simulations do not take gain-narrowing into account.

In order first to verify that orbits of the type shown in Fig. 7 determine the characteristic mode spacing of these cavities, Fig. 8 shows light scattering spectra for different sample sizes in the vicinity of the experimental wavelengths. Intensity is plotted versus dimensionless wavenumber kR, where $k = 2\pi/\lambda$. This is the natural scale for comparison with semiclassical predictions because modes differing by one node along a closed path should then be equally spaced, with a characteristic separation $\Delta(kR)_c = 2\pi R/(n L) = 2\pi/(3\sqrt{3}n) = 0.825$ independent of the sample size. The expected wavelength spacing of the modes (free spectral range FSR) is $\Delta\lambda = \lambda^2 \times \Delta(kR)_c/(2\pi R) \approx 23$ nm in (a) and $\Delta\lambda \approx 11$ nm in (b). For $WoF = 22$ μm, we obtain $\Delta\lambda \approx 4.9$ nm. Figure 8 indeed shows a series of resonant features with approximately the predicted wavevector spacing.

Each of the peaks marked in Fig. 8b is in fact a multiplet, which is not resolved because the splittings of the individual modes comprising the multiplet are smaller than their passive linewidths. There is evidence for this because several of the peaks are very asymmetric and in particular exhibit a steep slope on one side. For an isolated resonance, the most general lineshape that could arise is the Fano function (of which the Lorentzian is a special case), which however does not yield satisfactory fits here.

To further expose the multiplet structure, we modeled deviations from the ideal hexagonal shape which could lead to narrower individual linewidths and increase the multiplet splitting. Shape perturbations were chosen that preserve the D_{6h} point group symmetry and hence remove only "accidental" quasi-degeneracies. The actual perturbation that is present in the samples of Figs. 11 and 12 eluded experimental characterization, so that a model calculation can reproduce only generic features which are insensitive to the precise type of perturbation. One such feature is the *average* mode spacing after degeneracies have been lifted sufficiently.

Figure 9a shows the spectrum of a rounded hexagon where the radius of curvature at the corners is $\varrho \approx 0.9\,\lambda$ (assuming $\lambda \approx 610$ nm for definiteness). No qualitative difference from Fig. 8b is seen, except that the resonant features

Fig. 7. All four orbits shown have the same length and the same angle of incidence with respect to the interface normal, $\chi = 60°$. They hence satisfy the condition for total internal reflection, $\sin \chi > 1/n = 0.69$. In the case of rays impinging on the corners (rightmost picture) the ray picture breaks down
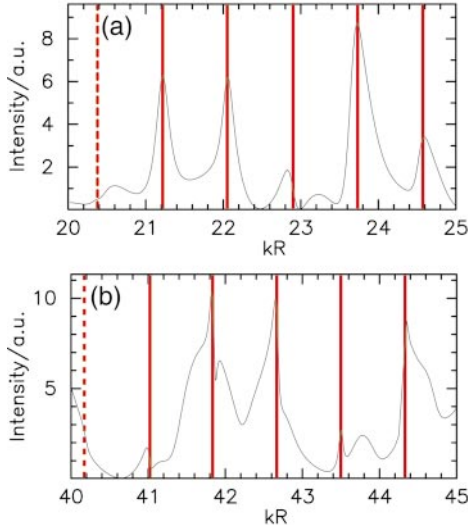
Fig. 8a,b. Calculated scattering intensity spectra of a hexagonal cylinder for plane-wave incidence at 15° to a side face and detection at 60° from incidence. **a** corresponds to a spectral interval $\lambda \approx 653–816$ nm for width over flats (*WoF*) 4.5 μm; **b** covers the interval $\lambda \approx 605–680$ nm for *WoF* 7.5 μm. *Vertical lines* are guides to the eye, indicating narrow resonances. The spacing between resonances is $\Delta(kR) \approx 0.84$ in **a** and $\Delta(kR) \approx 0.83$ in **b**, in good agreement with the characteristic mode spacing $\Delta(kR)_c \approx 0.83$ of a closed hexagonal orbit. Expected resonances not clearly seen in the above spectra are marked by *dashed lines*; they appear at other detection angles
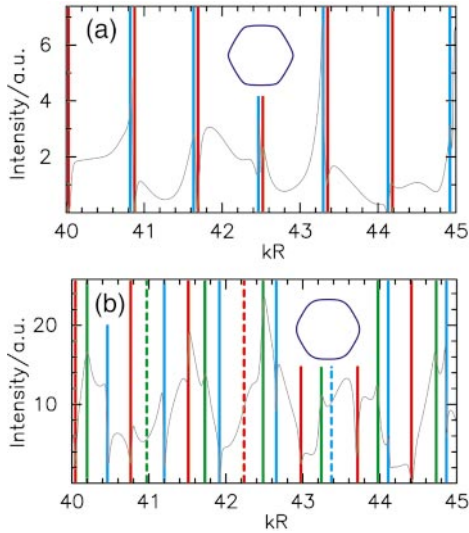

Fig. 9a,b. Calculated scattering intensity spectra for slightly rounded hexagonal cavities (shapes depicted as insets). The incoming plane wave is at an angle of 15° to a facet in **a** and 30° in **b**; detection occurs at 60° from incidence. Spacings between modes of the same color agree well with $\Delta(kR)_c \approx 0.83$, cf. Fig. 8. All resonances in **a** appear as doublets. At $kR \approx 42.5$ the doublet structure is seen most clearly. In **b**, stronger deviation from hexagonal shape leads to further lifting of degeneracies. *Dashed lines* mark expected resonances not seen at this observation angle

have become somewhat narrower, thus enabling us to identify two distinct series of modes with characteristic spacing $\Delta(kR)_c$. This indicates that departures from sharp corners are not resolved in the wave equation when their scale is smaller than λ. A qualitatively different spectrum is observed in Fig. 9b where $\varrho \approx 3.7\,\lambda$. Here, the perturbation reveals three well-separated, interpenetrating combs of modes, again

with period $\Delta(kR)_c$. There are 21 distinct resonances in the wavelength interval of Fig. 9b, which translates to an average mode spacing of $\Delta\lambda \approx 3.6$ nm for a *WoF* = 7.5 μm resonator, well in agreement with the experiment; cf. Fig. 12.

In order to verify that no further modes will be revealed by other choices of deformation, an independent estimate of the average density of modes can be made based on semiclassical considerations [35]:

$$\left\langle \frac{\mathrm{d}N}{\mathrm{d}(kR)} \right\rangle = \frac{n^2 kR}{4} \left[1 - \frac{2}{\pi} \left(\arcsin \frac{1}{n} + \frac{1}{n}\sqrt{1 - \frac{1}{n^2}} \right) \right]. \quad (1)$$

Here, $\mathrm{d}N$ is the number of modes in the interval $\mathrm{d}(kR)$. The result is $\left\langle \frac{\mathrm{d}N}{\mathrm{d}(kR)} \right\rangle \approx 4.6$, and hence we expect ≈ 22 modes in the interval of Fig. 9b, again in good agreement with the actual count.

2.3 Wave picture: intensity profile

There is one class of quasi-degeneracies that is not removed by any of the perturbations in Fig. 9: their physical origin is time-reversal symmetry for the ray motion inside the cavity. Any of the periodic orbits in Fig. 7 can be traversed either clockwise or counterclockwise, and the same holds for more general ray paths. The different propagation directions can be linearly combined in various ways to obtain nearly-degenerate standing-wave patterns that differ only in their parity with respect to some of the crystal's reflection axes. A minute splitting does exist because the non-integrability of
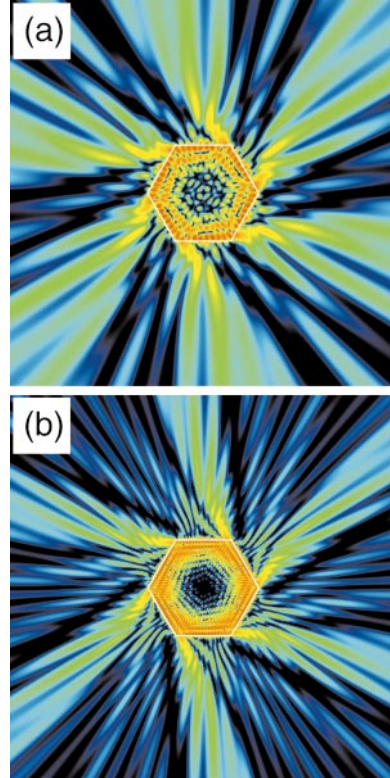

Fig. 10a,b. False-color representation of the cross-sectional intensity in the ideal hexagon for a mode with **a** $kR = 22.89$ [Fig. 8a] and **b** $kR = 42.78$ [Fig. 8b]. The resonance width is $\delta(kR) = 0.10$ in **a** and $\delta(kR) = 0.04$ in **b**

the ray motion implies that the propagation direction itself is not a "good quantum number", i.e. reversals of the sense of rotation are unlikely but not impossible in the wave equation. This is analogous to quantum tunneling and hence leads only to exponentially small splittings that can be neglected on the scale of the individual resonance linewidths [36]. These multiplets have been counted as one resonance in (1).

Following this reasoning, in Fig. 10 the *traveling-wave* patterns belonging to one of the resonances in Fig. 8a and b, respectively, is plotted. High-intensity ridges inside the resonator form a whispering-gallery-like pattern that decays from the interface into the cavity center. The number of ridges in the radial direction (perpendicular to a side face) provides an approximate analogue of a transverse mode order, however upon closer examination one sees that the number of ridges and nodal lines is not uniquely defined, in particular along a diameter joining opposite corners. The modes can therefore not be properly labeled by "good quantum numbers" characterizing the number of radial and azimuthal nodes — this is a direct consequence of the non-integrability of the problem. The most significant difference to the whispering-gallery modes of a circular cavity is clearly the anisotropic emission. High intensity is seen to emanate predominantly from the corners and is directed almost parallel to an adjacent crystal facet. The overall emission pattern is very similar in both modes despite the large difference in size (or kR) between the two hexagons.

3 Laser properties

The microcrystals were pumped with 10-ns pulses from the 532-nm second harmonic of a Nd:YAG laser delivered to the sample with an optical fiber. The emitted luminescence was collected with a $20\times$ microscope objective (collecting aperture $42°$) relaying the microlaser emission simultaneously to the spectrometer (cooled CCD-detector Oriel InstaSpecIV), and to the imaging system consisting of a cooled low-noise CCD-camera (PCO SensiCam). In Fig. 11 the emission and la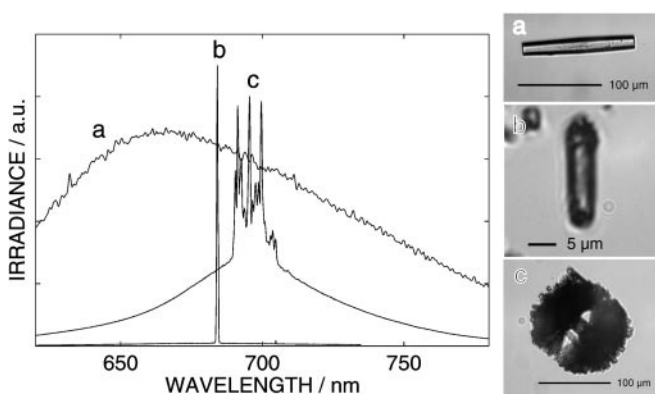sing spectra of different pyridine-2-loaded compounds are shown. With increasing dye content the fluorescence emission maximum of regularly shaped crystals shifted from 645 nm to 665 nm; cf. Fig. 11a. In none of these rod-shaped crystals was laser emission observed. However, narrow laser emission peaks (observed linewidth of 0.3 nm given by spectrometer resolution) occured in most fascicled samples. Emission maxima in these fascicled samples were observed at wavelenghts up to 695 nm, and again, increasing dye concentration correlated with increasing redshift (cf. Figs. 11b and c). As already mentioned, together with increasing dye content we also notice an increasingly disarranged crystal morphology. The observed facts, disturbed morphology and redshifted emission spectrum are consistent with the hypothesis of a host–guest interaction which increases with dye content. Essentially both, the pyridine-2 molecules and the $AlPO_4$-5 framework carry a static dipole moment [18, 19]. Obviously the buildup of electrostatic energy in the crystal lattice has to be compensated by an increasing amount of stacking faults. On the other side, the mechanism of the redshift is not unequivocally identified, yet, but is probably related to the one discussed in [37, 38].

The dye concentration in the rhodamine BE50-loaded $AlPO_4$-5 samples was around 75 unit cells per dye molecule, corresponding to 0.5 wt %. Also with these samples the same correlation between the emission wavelength and dye concentration was observed; cf. also [27]. In contrast to the pyridine-2-loaded samples, the fluorescence emission was not completely polarized. The observed polarization contrast $c_p = I_\parallel - I_\perp / I_\parallel + I_\perp$ was around 10%, indicating that on average the Rh BE50 molecules are only weakly aligned parallel to the crystal c-axis.

Independent of the type of loading, in most microcrystals with $WoF \gtrsim 8\,\mu m$ lasing was observed to occur on several sharp lines with instrument-resolution-limited width. A typical example is represented in Fig. 12. Note that the lines are not equally spaced. In fact, the free spectral range (FSR) of 11 nm corresponding to the resonator size is far above the observed line spacing of 3.2, 4.3, and 3.4 nm. This is in agreement with the theoretical model of Sect. 2.2, in which the average lasing mode spacing (after lifting the quasi-degeneracies in the ideal hexagon) was estimated to be $\Delta\lambda = 3.6$ nm. Also in agreement with the theoretical discussion are the emission regions where the laser light leaves the hexagonal resonators. Figure 13 (left) shows the laser
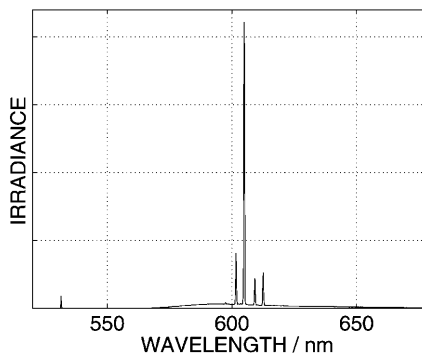
Fig. 11. Emission and lasing spectra of different pyridine-2-loaded compounds with from a to c increasing amounts of included dye. The dye concentration was estimated empirically based on the sample color depth. The width over flats of sample b is 4.5 μm. The free spectral range of this resonator is so large (about 24 nm) that one emission mode acquires the available gain resulting in single-line emission

Fig. 12. Lasing spectrum of a rhodamine BE50-loaded $AlPO_4$-5 microcrystal with a concentration around 75 unit cells per dye molecule and size of 7.5 μm width over flats
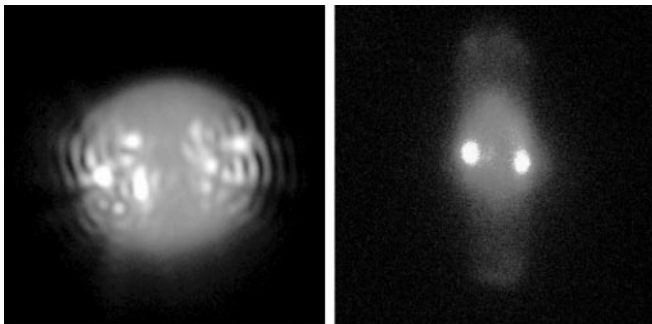
Fig. 13. Patterns of the laser emission show that the emission originates from regions along side edges. *Left*: rhodamine BE50/AlPO$_4$-5 compound; width over flats 7.5 µm. An electron micrograph of the sample is shown in Fig. 5 with horizontal *c*-axis. Here the *c*-axis orientation is nearly vertical. The corresponding emission spectrum is shown in Fig. 12. *Right*: pyridine-2/AlPO$_4$-5 compound; width over flats 4.5 µm. The corresponding sample and emission spectrum is represented in Fig. 11b

Fig. 14. Lasing threshold and differential efficiency of typical AlPO$_4$-5/dye compounds. Shown is the peak of the laser emission spectrum normalized by the fluorescence shoulder as a function of the pump power density for the sample shown in Figs. 11b and 12

emission as bright spots. Clearly the emission is concentrated along the crystal edges. The complex emission distribution is compatible with the simultaneously recorded spectrum (cf. Fig. 12) which reveals multimode emission.

On the other hand, samples with smaller resonator ($WoF \gtrsim 4$ µm), as for example the one shown in Fig. 11b emitted one single laser line. Therefore the emission is unadulterated by hole-burning-induced multimode beating and interference, and appears in the simple pattern shown in Fig. 13 (right), where two approximately 1-µm spots ($\approx$ microscope resolution limit) mark the region of laser emission, which, again, is located on the crystal edges. Compared with larger samples, the ratio of the line peak to the underlying fluorescence shoulder of these small lasers is an order of magnitude higher (cf. Fig. 14).

While, as described above, the average linespacing of 3.6 nm observed in the sample of Fig. 12 is not compatible with the free spectral range of $\Delta\lambda = 12$ nm of the corresponding resonator, the 4.2-nm spacing of the 3 dominant peaks in the sample shown in Fig. 11c is in accord with the *FSR* resulting from the 22-µm-*WoF* hexagonal resonator. The theoretical model for the 22-µm-*WoF* sample (cf. (1)) yields an average mode spacing of $\Delta\lambda \approx 0.5$ nm which is close to the spectrometer resolution. This high spectral density helps to explain the large background in the lasing spectrum of Fig. 11: it appears likely that not all the individual lasing modes in this sample were resolved, and hence part of the shoulder on which the three peaks of curve c sit is probably made up of other lasing modes. Any microcavity effects such as enhanced β factor (spontaneaous emission enhancement and suppression [39]) are also suppressed by the larger density of modes in the large sample.

Figure 14 illustrates the differential efficiency behavior of a typical microlaser with $WoF < 10$ µm and one with $WoF > 10$ µm. Lasing threshold for the latter size samples was around 0.5 MW/cm^2, regardless of the type of dye loading. On the other side, crystals of smaller size ($WoF = 4.5$ µm) from the same synthesis batch revealed a considerably smaller threshold (0.12 MW/cm^2) and a factor of > 7 larger differential gain. Wether this is a consequence of quantum size effects [39] will be clarified in progressing studies.

It is informative to compare the threshold of molecular sieve microlasers with vertical cavity surface-emitting lasers
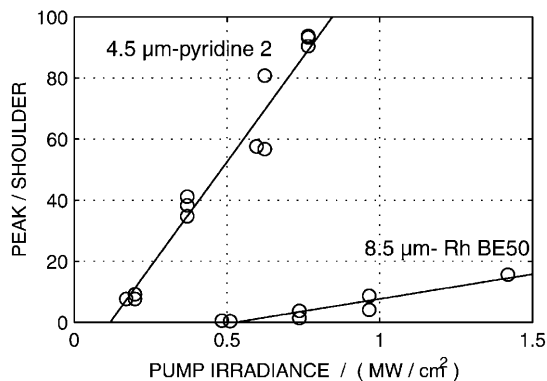
(VCSELs). VCSELs with a size comparable to sample b in Fig. 11 exhibit threshold currents of about 1 mA, which corresponds to 6.25×10^{15} s^{-1} electrons. On the other hand, the threshold power density of 0.12 MW/cm^2 incident on the molecular sieve laser surface of 1×4.5 µm (cf. Fig. 13) corresponds to a current of 1.4×10^{16} s^{-1} 532-nm-photons, or a factor of 2.24 over the electron rate. As the pump radiation is not polarized but the molecular ensemble of the considered laser is aligned, only half of the pump photons actually contribute to the inversion. Thus, in terms of elementary (quantum) pump processes needed to reach lasing threshold the molecular sieve lasers are comparable to VCSELs.

4 Photostability

Photostability is a critical issue with dye lasers. We investigated samples exhibiting an undisturbed morphology, similar to the one shown in Fig. 1. The pyridine-2-loaded samples were irradiated with 10 Hz trains of 10 ns pulses of the 532-nm second harmonic of a Nd:YAG laser and a power density of 5 MW/cm^2. Figure 15 illustrates the dwindle of fluorescence activity of a pyridine-2-loaded AlPO$_4$-5 sample under such bleaching irradiation. After a bleaching period of 140 s the exposure was interrupted for 18 min. Then the
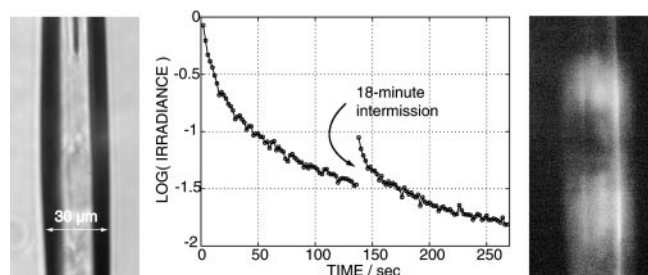

Fig. 15. Fluorescence activity of a pyridine-2-loaded AlPO$_4$-5 sample under bleaching laser irradiation. *Left*: Micrograph of the sample crystal. *Center*: Fluorescence activity as a function of time: After a first bleach period of 140 s the bleach beam is interrupted for 18 min. During this intermission the fluorescence recovers to start the second bleach period with 3× stronger emission. *Right*: The bleaching laser is incident from the left and concentrated in the center of the crystal. Shown is the fluorescence distribution at the end of the first bleach period of 140 s. Clearly visible is the bleached hole in the center, where the bleach beam was concentrated

bleaching procedure was resumed. Apparently the fluorescence recovers during the intermission. If it is assumed that bleaching consists in breaking bonds of the dye molecules, then bond energies in the eV range have to be considered. Even if the dye debris might remain encaged in their pores, spontaneous or thermally activated self healing of broken eV-bonds seems not very probable. One can therefore suppose that the recovery is due to diffusion of new, intact dye molecules into the bleached volume. Considering the stereometrically restricted possibilities inside the molecular sieve framework together with diffusion distances of several μm and the observed recovery time in the range of minutes, diffusion is more plausible than self-healing.

As bleaching reduces the concentration of dye, a blueshift of the fluorescence is expected with increasing photobleaching [18, 19]. However, the 656-nm-fluorescence emission maximum of this sample is already at the shortest observed wavelength (cf. Fig. 11), corresponding to a low dye concentration, and consequently, to weak dipole interactions. Thus, the blueshift under these circumstances must be rather small. This explains the fact that we could not detect a measurable blueshift with these pyridine-2-loaded samples.

On the other hand, the rhodamine BE50-loaded samples under investigation contained dye at a concentration of around one Rh BE50 molecule per 75 unit cells, and therefore bleaching caused a detectable 4-nm shift of the fluorescence towards the blue (bleach irradiance $0.5\,\mathrm{MW/cm^2}$). Observing the laser emission spectrum while bleaching the samples, a further consequence of the blueshift was revealed: blueshift of the fluorescence reduces the overlap of the fluorescence band with the absorption spectrum, and as a result laser modes at lower wavelengths will suffer fewer losses with increasing bleaching. This is documented in Fig. 16, where the intensity of mode b with the shortest oscillating wavelength increases, while longer-wavelength-modes a and c decrease during the bleach procedure. At the same time a 0.2-nm blueshift of the oscillation wavelength was detected. We attribute this to a weak decrease of the refractive index of the resonator material due to the smaller polarizability of the dye debris. In contrast to the pyridine-2 samples, however, recovery of the fluorescence was not detected. As the Rh 50BE molecules are considerably larger than pyridine-2 molecules their mobility in the molecular sieve framework is severly hampered. So, diffusion of intact molecules into the bleached volume occurs — if ever — on larger timescales than minutes.

5 Conclusion

We have reported about a new form of microlasers based on nanoporous molecular sieves containing embedded dyes. Size- and shape-dependent laser properties were observed, in agreement with theoretical predictions: Larger hexagonal crystals ($WoF \gtrsim 10\,\mu\mathrm{m}$) revealed multiline laser emission, while the smaller ones ($WoF \approx 5\,\mu\mathrm{m}$) oscillate on one single line. The laser threshold power density of these small lasers is approximately a factor of 3 lower than the threshold of $WoF \approx 10\,\mu\mathrm{m}$–lasers, and their differential efficiency is almost an order of magnitude larger. Although these properties did not depend on the type of embedded dye molecules, the photostability seems to be affected by the size of the molecules. Molecules that fit into the pores, such as pyridine 2, keep the ability to diffuse in the pore framework of the molecular sieve. Therefore photobleached molecules can be replaced by intact ones diffusing into the luminescing volume.

Fig. 16. Effect of photobleaching on the laser emission intensity: short wavelength line b grows with progressive bleaching, while longer wavelength lines a and c decrease

References

1. M. Rifani, Y.Y. Yin, D.S. Elliot, M.J. Jay, S.H. Jang, M.P. Kelley, L. Bastin, B. Kahr: J. Am. Chem. Soc. **117**, 7572 (1995)
2. B. Kahr, S.H. Jang, J.A. Subramony, M.P. Kelley, L. Bastin: Adv. Mater. **8**, 941 (1996)
3. F.J. Duarte: Opt. Commun. **117**, 480 (1995)
4. S. Popov: Appl. Opt. **37**, 6449 (1998)
5. U. Vietze, O. Krauß, F. Laeri, G. Ihlein, F. Schüth, B. Limburg, M. Abraham: Phys. Rev. Lett. **81**, 4628 (1998)
6. G.D. Stucky, J.E. Mac Dougall: Science **247**, 669 (1990)
7. G. Schulz-Ekloff: in *Advanced Zeolite Science and Applications*, ed. by J.C. Jansen, M. Stöcker, H.G. Karge, J. Weitkamp Vol. 85, Stud. Surf. Sci. Catal. (Elsevier, Amsterdam 1994) p. 145
8. S.D. Cox, T.E. Gier, G.D. Stucky, J. Bierlein: J. Am. Chem. Soc. **110**, 2986 (1988)
9. N. Gfeller, S. Megelski, G. Calzaferri: J. Phys. Chem. B **102**, 2433 (1998); J. Phys. Chem. B **103**, 1250 (1999)
10. M. Bredol, U. Kynast, C. Ronda: Adv. Mater. **3**, 361 (1991)
11. I. Braun, M. Bockstette, G. Schulz-Ekloff, D. Wöhrle: Zeolites **19**, 128 (1997)
12. K. Hoffmann, F. Marlow, J. Caro: Adv. Mater. **9**, 567 (1997)
13. W.M. Meier, D.H. Ohlson, C. Baerlocher: *Atlas of Zeolite Structure Types* (Elsevier, London 1996), cf. also the URL: http://www.iza-sc.ethz.ch/IZA-SC/Atlas/AtlasHome.html
14. S.T. Wilson: in *Introduction to Zeolite Science and Practice*, ed. by H. van Bekkum, E.M. Flanigen, J.C. Jansen, Vol. 58, Stud. Surf. Sci. Catal. (Elsevier, Amsterdam 1991) p. 137
15. I. Girnus, K. Jancke, R. Vetter, J. Richter-Mendau, J. Caro: Zeolite **15**, 33 (1995); I. Girnus, M. Poll, J. Richter-Mendau, M. Schneider, M. Noack, D. Venzke, J. Caro: Adv. Mater. **7**, 711 (1995)
16. S.A. Schunk, D.G. Demuth, B. Schulz-Dobrik, K.K. Unger, F. Schüth: Microporous Mater. **6**, 273 (1996); Ö. Akdogan, G. Ihlein, F. Schüth: Microporous Mesoporous Mater. in press
17. H. Du, M. Fang, W. Xu, X. Meng, W. Pang: J. Mater. Chem. **7**, 551 (1997)
18. J.M. Bennett, J.R. Cohen, E.M. Flanigen, J.J. Pluth, J.V. Smith: in *Intrazeolite Chemistry*, ed. by G.D. Stucky, F.G. Dwyer, Vol. 218, ACS Symp. Series (Am. Chem. Soc., Washington DC 1983) p. 109
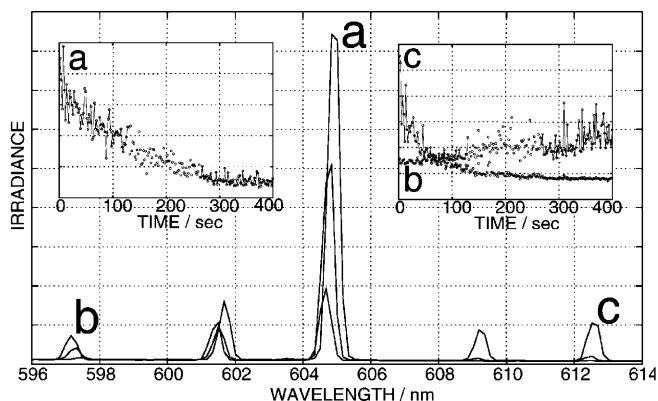
19. J.A. Martens, P.A. Jacobs: in *Advanced Zeolite Science and Applications*, ed. by J.C. Jansen, M. Stöcker, H.G. Karge, J. Weitkamp, Vol. 85, Stud. Surf. Sci. Catal. (Elsevier, Amsterdam 1994) p. 653

20. G.J. Klap, S.M. van Klooster. M. Wübbenhorst. J.C. Jansen, H. van Bekkum, J. van Turnhout: in *Proc.* 12th *Intern. Zeolite Conf.*, ed. by M.M.J. Treacy, B.K. Marcus, M.E. Bisher, J.B. Higgins (Materials Research Society, Warrendale (PA) 1999), Vol. 3, p. 2117

21. U. Brackmann: *Lambdachrome Laser Dyes* (Lambda Physik, Göttingen 1994) p. 198

22. R. Hoppe, G. Schulz-Ekloff, D. Wöhrle, E.S. Shpiro, P.P. Tkachenko: Zeolites **13**, 222 (1993)

23. D. Demuth, G.D. Stucky, K.K. Unger, F. Schüth: Microporous Mater. **3**, 473 (1995)

24. G. Ihlein, F. Schüth, O. Krauß, U. Vietze, F. Laeri: Adv. Mater. **10**, 1117 (1998)

25. S.T. Wilson, B.M. Lok, C.A. Messina, T.R. Cannan, E.M. Flanigen: J. Am. Chem. Soc. **104**, 1146 (1982)

26. S. Wohlrab, R. Hoppe, G. Schulz-Ekloff, D. Wöhrle: Zeolites **12**, 862 (1992); D. Wöhrle, A.K. Sobbi, O. Franke, G. Schulz-Ekloff: Zeolites **15**, 540 (1995)

27. M. Bockstette, D. Wöhrle, I. Braun, G. Schulz-Ekloff: Microporous Mesoporous Mater. **23**, 83 (1998)

28. I. Braun, G. Schulz-Ekloff, G. Schnurpfeil. D. Wörle, K. Hoffmann: in preparation

29. I. Braun, G. Schulz-Ekloff, D. Wöhrle, W. Lautenschläger, Microporous Mesoporous Mater. **23**, 79 (1998)

30. A. Mekis, J.U. Nöckel, G. Chen, A.D. Stone, R.K. Chang: Phys. Rev. Lett. **75**, 2682 (1995)

31. J.U. Nöckel, A.D. Stone: Nature **385**, 45 (1997)

32. C. Gmachl, F. Capasso, E.E. Narimanov, J.U. Nöckel, A.D. Stone, J. Faist, D.L. Sivco, A.Y. Cho: Science **280**, 1556 (1998)

33. P.J. Richens, M.V. Berry: Physica D **2**, 495 (1981)

34. A. Hobson: J. Math. Phys. **16**, 2210 (1975)

35. J.U. Nöckel, A.D. Stone: unpublished

36. M.J. Davis, J.E. Heller: J. Chem. Phys. **75**, 246 (19981)

37. T. Förster: Z. Naturforsch. A **4**, 321 (1949)

38. T. Förster: *Fluoreszenz Organischer Verbindungen* (Vandenhoeck & Ruprecht, Göttingen 1951) p. 139ff

39. Y. Yamamoto: in *Quantum Optics of Confined Systems*, ed. by M. Ducloy, D. Bloch (Kluwer, Dordrecht 1996) p. 241ff